



Numerical modeling from process to residual stress induced in resistance spot welding of DP980 steel

Sendong Ren^{1,2} · Wenjia Huang¹ · Ninshu Ma¹ · Goro Watanabe³ · Zhengguang Zhang³ · Wenze Deng³

Received: 14 August 2022 / Accepted: 9 January 2023 / Published online: 2 February 2023
© The Author(s), under exclusive licence to Springer-Verlag London Ltd., part of Springer Nature 2023

Abstract

DP980 is widely used in automotive bodies. In the present research, a numerical model was developed via the in-house finite element (FE) code JWRIAN-RSW for the multi-physics coupled process of resistance spot welding (RSW) of DP980 sheets and JWRIAN-Hybrid for residual stress. The high-temperature material properties and metallurgical behaviors of DP980 were clarified via experiment to ensure simulation accuracy. The measured thermal expansion curve indicated the austenite and martensite transformation in DP980 and clarified the critical temperatures. Material properties such as thermal expansion and stress-strain curves in heating and cooling processes were measured. The double-pulse electric current mode in RSW was employed and it was found that the molten zone disappeared temporarily between two current pulses. The final dimension of welding nugget was determined by the second pulse. The volume expansion of martensite transformation led to a clear stress drop (about 400MPa) in the welding nugget and heat-affected zone. The final value of X-stress and Y-stress on the center of surface was about 300MPa and 240MPa, respectively. Except for the solid-state phase transformation, the springback process also had a significant influence on residual stress, which cannot be ignored in numerical modeling. The predicted temperature field and residual stress distribution showed good agreement with the molten zone morphology and XRD measurements, which demonstrated the effectiveness of developed FE model.

Keywords Resistance spot welding · Residual stress · Numerical modeling · Martensite transformation · Springback · DP980

1 Introduction

Lightweight design is always a challenging topic in the automobile industry since lightweight production can realize less fuel consumption. Compared with structural design optimization, material substitution is a more prevalent choice due to cost and time consumption [1]. Recently, the advanced high strength steel (AHSS) has been a promising material as a substitute for traditional iron and steel in the automobile

industry. Depending on its high weight-to-strength ratio and excellent crashworthiness [2], the AHSS can significantly reduce the total weight of body-in-white and ensure the required strength at the same time. Meanwhile, resistance spot welding (RSW) is the most common joining technology for assembling sheet structures in vehicles, which has a hundred years of history [3]. The RSW process is characterized by low unit cost, good operability, and simple equipment requirements. In the modern automobile industry, a mass production can contain thousands of RSW joints. Therefore, the quality of body-in-white is mainly determined by the RSW process.

Several researches have investigated the factors those influence the quality of the resistance spot welds. Nugget size is reported as a critical factor that determines the overall mechanical properties of RSW joints [4]. Vijayan et al. [5] discussed the effect of welding current in the DP780 RSW joint. The increased welding current resulted in a larger nugget diameter. Ashiri et al. [6] designed a double-pulse RSW process to join Zn-coated steel. The first pulse was

✉ Sendong Ren
rensensong@zjut.edu.cn

✉ Ninshu Ma
ma.ninshu@jwri.osaka-u.ac.jp

¹ Joining and Welding Research Institute, Osaka University, 11-1, Mihogaoka, Ibaraki, Osaka 567-0047, Japan

² College of Mechanical Engineering, Zhejiang University of Technology, Hangzhou 310014, Zhejiang, China

³ Geely Automobile Research Institute (Ningbo) Co., Ltd., Ningbo 315336, Zhejiang, China

employed to generate minimum nugget size and the second one was used to increase diameter. Li et al. [7] used magnetically assisted resistance spot welding to improve the weld quality of DP590. Both quasi-static mechanical properties and fatigue life were improved with the notably increased nugget size. Ren et al. [8] designed a novel ceramic-filled annular electrode for the RSW of DP980 steel. The nugget area increased to 69 mm² and the maximum failure load reached 22.9 kN in the tensile shear test. Other researchers pay more attention to the welding residual stress in RSW joints. Yang et al. [9] proposed that the welding residual stress near nugget was the major factor that affected fatigue life. Sato et al. [10] measured the welding residual stress on DP590 RSW joint via X-ray diffraction (XRD) method. A clear stress drop was detected at the edge of indentation induced by electrode. Tensile stress located at the center of nugget surface. Chabok et al. [11] investigated the single- and double-pulse RSW process on DP1000-GI steel. There was a lower compressive stress perpendicular to the plane pre-crack in double pulse-welded sample, which led to the poor mechanical performance.

In order to optimize the process parameters effectively, the finite element method (FEM) has been widely accepted in academic and engineering applications. Moshayedi and Sattari-Far [12] established a 2D model based on ANSYS to reproduce the nugget growth on 304L RSW joints. Both welding current and time had a positive effect on the increase of nugget before the expulsion appeared. Wan et al. [13] simulated the dissimilar material RSW process between Al- and zinc-coated steel. The nuggets' size in different materials can be predicted accurately by considering the detail of contact conditions. Ma and Murakawa developed a 2D model to predict the welding nugget dimensions and nugget formation processes on the three pieces of high-strength steel RSWed joints [14]. Lee et al. [15] proposed a 3D finite element (FE) model in ABAQUS to predict the nugget diameter on SPRC 340 RSW joints. The mean absolute percent error was less than 3.80%. Wang et al. [16] studied the effect of electrode shape on RSW quality of DP590 steel. Some 2D FE models with different electrode tips were created in ABAQUS software to predict the molten zone morphology. Zhao et al. [17] modeled the RSW process of DP600. Their study just focused on the prediction of nugget size; hence, the metallurgical behavior of metal was ignored in the numerical model. Feujofack Kemda et al. [18] modeled the phase transformation kinetics in AISI 1010 during RSW process. The temperature field and phase distribution were predicted while their study did not investigate the welding residual stress. Besides, Iyota et al. [19] examined the effect of martensitic transformation on the residual stress of HT980 RSWed joint based on SYSWELD. They proposed that considering the change in yield strength and thermal expansion was necessary to predict residual stress accurately. Pakkanen et al. [20]

established an axisymmetric model in SYSWELD to predict the welding residual stress distribution on DP1000 RSW joint. The solid-state phase transformation (SSPT) was taken into account to describe the metallurgical behavior of materials. The simulated stress field showed a similar tendency with measurement, but there was still a large discrepancy in the magnitude of residual stress.

Although the 2D axisymmetric FE model can be accepted for the numerical simulation of RSW, it is no doubt that the full-scale 3D model can provide more accurate results by considering the detailed boundary conditions. Meanwhile, the SSPT is a critical metallurgical behavior in dual-phase steel, which influences the evolution of welding residual stress significantly [21]. Besides, the high-temperature material properties and the consideration of springback process are also necessary to ensure the prediction accuracy of FE model. However, these are rarely reported currently.

In the present research, the DP980 steel was joined via resistance spot welding. The SSPT process and high-temperature material properties of DP980 were measured. The multi-physics coupling process of RSW was realized based on the in-house FEM software JWRIAN. The springback process was also taken into account. A full-scale FE model was established to perform the numerical analysis. The predicted temperature field and residual stress distribution were verified by comparing with the molten zone morphology and XRD measurement, respectively.

2 Experimental procedure

2.1 Material and welding process

The HC550/980DP steel was used in the current research. The overall dimension of steel sheet was 125mm × 38mm × 1.2mm. Two sheets were overlapped completely and welded at the center. The RSW experiment was performed via a robot-type direct current welding machine with a couple of CuCr electrodes. The surface diameter and spherical radius of electrodes were 6 mm and 40 mm, respectively. The time-dependent welding current and electrode force are illustrated in Fig. 1. The first current pulse was designed with a large current and short time. The metal closed to the interfaces would be heated and softened rapidly thereby improving the interfacial contact condition. After a short interval, the second pulse with a low current was used to support the steady growth of welding nugget.

2.2 Metallurgical test

The welding nugget (WN), heat-affected zone (HAZ), and base metal (BM) on the cross-section of RSWed joint were distinguished via the metallurgical test. A sample included

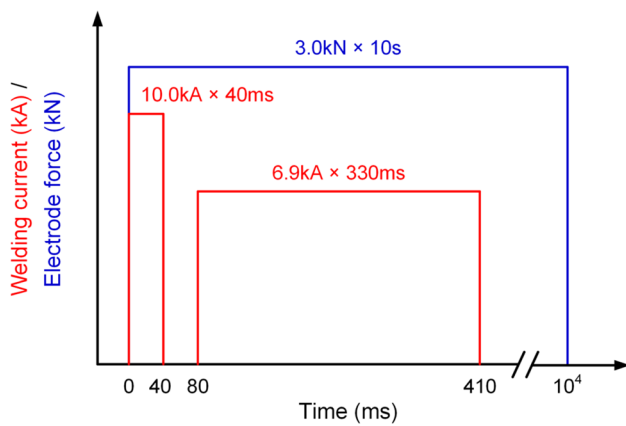


Fig. 1 Time-dependent welding current and electrode force

above subregions was cut in transverse direction by wire electrical discharge machining, then mounted in resin, polished following standard procedure, and etched using 4% Nital solution. The optical observation of cross-section was performed on the KEYENCE V-Z20R digital microscope.

2.3 Welding residual stress measurement

The μ -X360s portable residual stress analyzer made by PULSTIC was employed to measure the welding residual stress distribution on the top surface of welded joint. The measurement path is depicted in Fig. 2. The incidence angle of X-ray for ferrite was set as 35° . The measuring points were distributed within a space of 2 mm. It should be mentioned that the initial stress in DP980 sheet was gauged as about -40MPa . It was ignored in the numerical modeling since its magnitude was slight compared with welding residual stress.

2.4 High-temperature material properties measurement

The critical temperature points of SSPT in DP980 and the thermal expansion-temperature curve were clarified via an automatic dilatometer (Formastor-EDP). The sample was machined to a cuboid of $1.2\text{mm} \times 2.0\text{mm} \times 10.0\text{mm}$ and subjected to a thermal cycle in vacuum. The designed thermal cycles are given in Fig. 3. The microstructure in raw

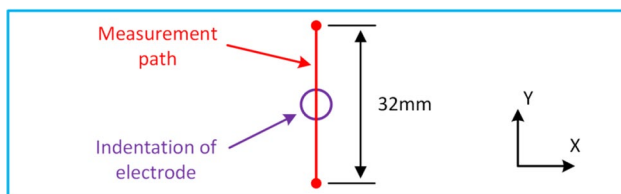


Fig. 2 XRD measurement path

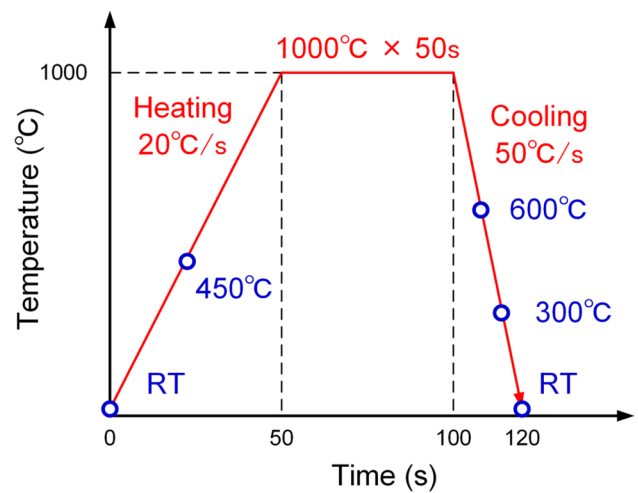


Fig. 3 Designed thermal cycle and the typical points for high-temperature tensile tests

metal and after heat treatment were observed via an optical microscope.

In order to clarify the yield strength and work hardening behaviors of distinct phases, the high-temperature tensile test was processed subsequently on a universal material testing machine AG-100kNE. The preset test conditions were also marked as blue circles in Fig. 3. A total of five tensile specimens were fabricated according to the JIS Z 2201:1998 standard (size no. 5) [22]. For each experiment, the sample was subjected to the designed thermal cycle in nitrogen atmosphere, held on 50s at the target temperatures and then started tensile test. The strain rate was set as $2 \times 10^{-3}/\text{s}$. Direct-contact extensometer was employed and the gauge length was 30mm.

3 Numerical modeling

3.1 Numerical simulation procedure

Generally, some commercial software can provide an interface for engineers to simulate the welding process and solve manufacturing problems. While from the academic viewpoint, developing in-house FE code can give deeper and more detailed understanding for the modeling process. Resistance spot welding is a multi-physics coupling process. In the previous research, the numerical simulation was processed based on the in-house FEM software JWRIAN [23], which flowchart is illustrated in Fig. 4. Two program modules were called in sequence. Firstly, the JWRIAN-RSW was employed to reproduce the electrical-thermal-mechanical coupling process, a detailed consideration of dynamic contact conditions ensures the analysis accuracy [24]. The electrical analysis was employed to calculate the electric

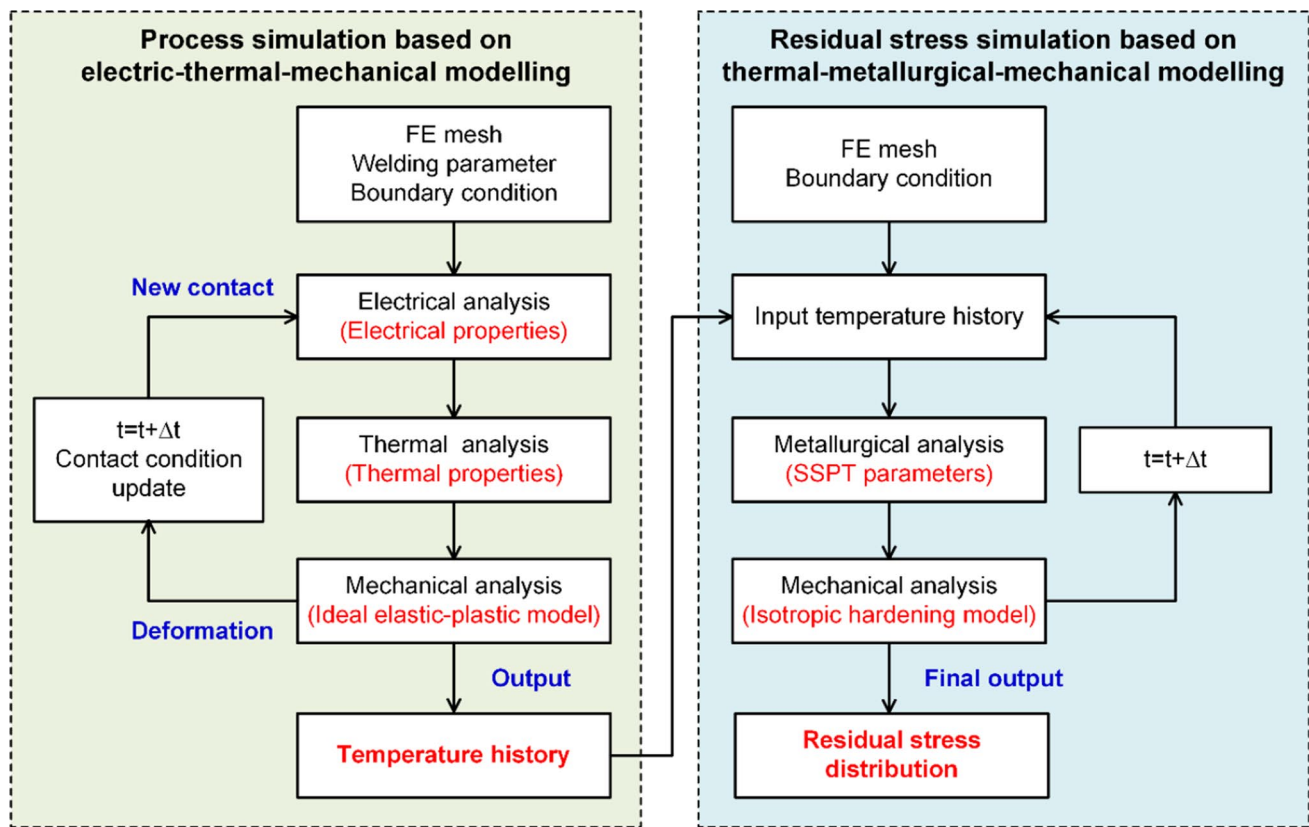


Fig. 4 Flowchart of the numerical simulation procedure in JWRIAN

field and Joule heat generation. Then thermal analysis can consider the transient heat transfer to predict the temperature field. The deformation was obtained from the mechanical analysis with considering the ideal elastic-plastic material behavior, which was employed to perform the contact judgment and define new contact conditions in the next timestep [25]. Finally, the temperature history of the entire FE model was recorded and output for the continuous simulation. It should be mentioned that the welding current can introduce an induced magnetic field during the RSW process [26, 27]. The proposed model ignored this phenomenon since it was not the primary factor for RSW process.

The JWRIAN-Hybrid was used to perform thermal-metallurgical-mechanical analysis [28, 29]. It should be mentioned that the thermal analysis was substituted by inputting the temperature history directly. The thermal information was assigned to the whole model rather than performed iterative calculation. Thereby, the simulation efficiency was improved significantly. Then the metallurgical analysis was used to consider the detail of SSPT process, including the volume change and yield strength variation. The mechanical analysis can regard the detailed work hardening behavior of distinct phases in different temperatures. Considering the rapid heating and cooling of RSW process, the annealing

effect was ignored in the FE model. The welding residual stress distribution can be calculated accurately at the end of simulation. Especially, the springback process was taken into account in the numerical modeling, which presented the uniqueness of our research.

3.2 Multi-physics coupling model

In the Cartesian coordinate system, the static electric field can be described via the Laplace's equation:

$$\frac{\partial}{\partial x} \left(\frac{1}{R} \cdot \frac{\partial \phi}{\partial x} \right) + \frac{\partial}{\partial y} \left(\frac{1}{R} \cdot \frac{\partial \phi}{\partial y} \right) + \frac{\partial}{\partial z} \left(\frac{1}{R} \cdot \frac{\partial \phi}{\partial z} \right) = 0 \quad (1)$$

where R [$\Omega \cdot \text{mm}$] was the electrical resistivity of materials.

The electrical potential $\{\phi\}$ can be calculated according to the electrical matrix $[E]$ and pre-described welding current vector $\{\bar{I}\}$:

$$[E]\{\phi\} = \{\bar{I}\} \quad (2)$$

Then the components of current density i [$\text{A} \cdot \text{mm}^{-2}$] are calculated:

$$i_x = \frac{1}{R} \cdot \frac{\partial \varphi}{\partial x}, i_y = \frac{1}{R} \cdot \frac{\partial \varphi}{\partial y}, i_z = \frac{1}{R} \cdot \frac{\partial \varphi}{\partial z} \tag{3}$$

The internal volume heat generation rate q_v [$J \cdot mm^{-3} \cdot s^{-1}$] is solved according to the Joule’s law:

$$q_v = (i_x^2 + i_y^2 + i_z^2)R \tag{4}$$

The partial differential equation for calculating transient temperature field is defined by:

$$\rho c \frac{\partial T}{\partial t} = \frac{\partial}{\partial x} \left(\lambda \frac{\partial T}{\partial x} \right) + \frac{\partial}{\partial y} \left(\lambda \frac{\partial T}{\partial y} \right) + \frac{\partial}{\partial z} \left(\lambda \frac{\partial T}{\partial z} \right) + q_v \tag{5}$$

where ρ , c , and λ represent the density [$g \cdot mm^{-3}$], and specific heat capacity [$J \cdot g^{-3} \cdot ^\circ C^{-1}$] as well as thermal conductivity [$J \cdot mm^{-1} \cdot ^\circ C^{-1} \cdot s^{-1}$], respectively.

The transient temperature $\{T\}$ and its rate $\{\partial T/\partial t\}$ are given as:

$$[S]\{T\} + [C]\left\{\frac{\partial T}{\partial t}\right\} = \{Q\} \tag{6}$$

where $[S]$ and $[C]$ express the thermal conductivity and heat capacity matrix, respectively. $\{Q\}$ is the heat flux.

The transient temperature can be discretized as :

$$\frac{\partial T}{\partial t} = \frac{(T_{t+\Delta t} - T_t)}{\Delta t} = \theta \cdot \left(\frac{\partial T}{\partial t}\right)_{t+\Delta t} + (1 - \theta)\left(\frac{\partial T}{\partial t}\right)_t \tag{7}$$

where Δt is the time step, and $\theta \in [0, 1]$ is a weighting factor.

In this study, the value of θ was defined as 0.5 and the Crank-Nicolson method was employed to solve transient temperature field:

$$\left(\frac{1}{2}[S] + \frac{[C]}{\Delta t}\right)\{T\}_{t+\Delta t} = \frac{1}{2}(\{Q\}_{t+\Delta t} + \{Q\}_t) + \left(\frac{[C]}{\Delta t} - \frac{1}{2}[S]\right)\{T\}_t \tag{8}$$

In the mechanical analysis, the nodal displacement vector $\{\Delta u\}$ can be solved from the governing equation:

$$[K]\{\Delta u\} = \{\Delta F\} + \{P\} \tag{9}$$

where $[K]$ is the stiffness matrix; $\{\Delta F\}$ and $\{P\}$ represent the vector of force and stress on structural nodes, respectively.

Considering the influence of SSPT, the total strain increment $\{\Delta \epsilon\}$ can be written as:

$$\{\Delta \epsilon\} = [B]\{\Delta u\} \tag{10}$$

$$\{\Delta \epsilon\} = \{\Delta \epsilon^e\} + \{\Delta \epsilon^T\} + \{\Delta \epsilon^p\} + \{\Delta \epsilon^{ph}\} \tag{11}$$

where $[B]$ matrix describes the relationship between strain and internal nodal displacements. $\{\Delta \epsilon^e\}$, $\{\Delta \epsilon^T\}$, $\{\Delta \epsilon^p\}$, and

$\{\Delta \epsilon^{ph}\}$ express the increment of elastic strain, thermal strain, plastic strain, and phase transformation–induced volume strain, respectively. For simplicity, the $\{\Delta \epsilon^p\}$ and $\{\Delta \epsilon^{ph}\}$ were equivalently considered from the measured true stress-effective plastic strain curve and thermal expansion curve, respectively.

Finally, the stress $\{\sigma\}$ is computed according to the thermal-elastic-plastic theory:

$$\{\sigma\}_{t+\Delta t} = \{\sigma\}_t + \{\Delta \sigma\} \tag{12}$$

$$\{\Delta \sigma\} = [D]\{\Delta \epsilon^e\} \tag{13}$$

where $\{\Delta \sigma\}$ is the stress increment, and $[D]$ is the elastic matrix.

3.3 FE mesh and boundary conditions

A full-scale 3D FE mesh was established for the RSW structure, as shown in Fig. 5. The number of structural nodes and 8-node solid elements was 22,160 and 19,280, respectively. The minimum element size in the expected welding nugget was $0.2mm \times 0.2mm \times 0.3mm$.

The electrical, thermal, and mechanical boundary conditions of RSW process are illustrated in Fig. 6. Electrode force and welding current were applied to the ring region of top electrode, in which the structural nodes were also fixed on X and Y directions. The ring region of bottom electrode was set as the potential boundary, where the voltage value was defined as zero. And the related nodes were fixed on three directions. Meanwhile, the internal surfaces of two electrodes were set as the thermal boundary condition. The temperature of thermal boundary was defined as $20^\circ C$ to consider the cooling effect of circulating water.

3.4 Material properties

The material properties required for FEM analysis included electrical resistivity R [$\Omega \cdot mm$], thermal conductivity λ [$J/(mm \cdot ^\circ C \cdot s)$], specific heat c [$J/(g \cdot ^\circ C)$], density ρ [g/cm^3], Poisson’s ratio ν , Young’s modulus E [GPa], yield strength YS [MPa], and the coefficient of thermal expansion (CTE)

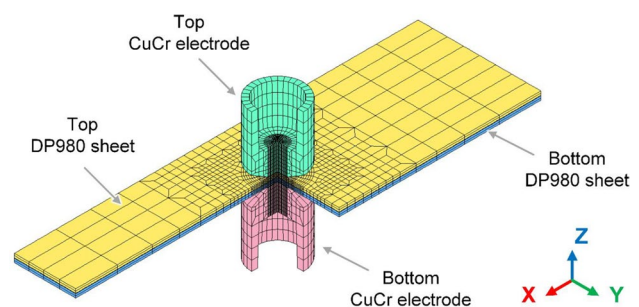


Fig. 5 3D-FE mesh for the RSW structure

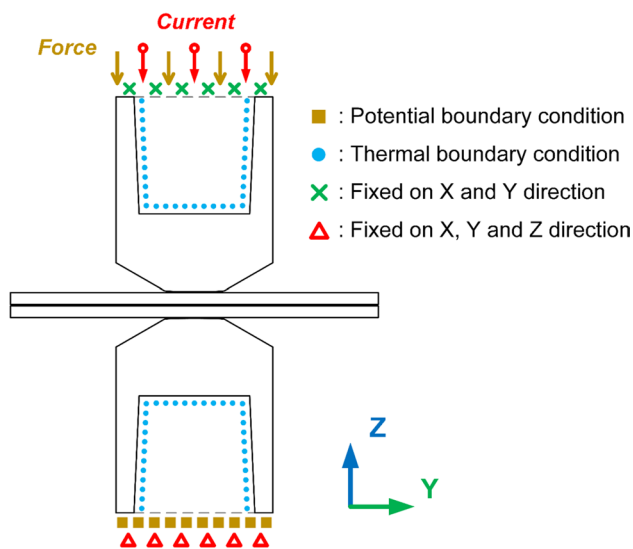


Fig. 6 Schematic diagram of the boundary conditions

α [$1/^\circ\text{C}$]. In the present research, the yield strength and CTE of DP980 were clarified by experiment to consider the effect of SSPT. Other temperature-dependent material properties of CuCr and DP980 were cited from references and listed in Table 1 and Table 2, respectively.

4 Results and discussion

4.1 SSPT and high-temperature material properties of DP980

The measured thermal expansion curve of DP980 is shown in Fig. 7. Obviously, the SSPT had a significant effect on the strain variation during thermal cycle, which was well known

as the volume change [30]. The initial phase of DP980 at room temperature was martensite and ferrite, which has body-centered tetragonal (bct) and body-centered cubic (bcc) structures, respectively [31]. The metal was heated and expanded until the cementite disappearance temperature (Ac_1) [32]. The phase started to transfer into austenite with a face-centered cubic (fcc) structure. Thereby, one can observe an evident strain shrinkage. The austenite transformation was finished when temperature reached the α -ferrite disappearance temperature (Ac_3). The volume of austenite trended to increase during the continuous heating. In the present research, the Ac_1 and Ac_3 for DP980 were detected as 760°C and 850°C , respectively.

During the cooling stage, the phase of DP980 was kept in austenite before the martensite transformation started. Once the temperature decreased to martensite start (M_s) temperature, the microstructure was altered into martensite again and induced a significant volume expansion. The martensite transformation was finished at the martensite finish (M_f) temperature. When the metal cooled to room temperature, the negative value of strain demonstrated that the SSPT in DP980 can generate compressive stress during the welding process. The M_s and M_f points of DP980 were clarified as 420°C and 340°C , respectively.

Besides, the mathematical model of martensite transformation was relatively simple, which can be described via the Koistinen-Marburger (K-M) relationship [33]:

$$f = 1 - \exp[-b(M_s - T)] \quad (14)$$

where f was the fraction of martensite at current temperature, and b was the law parameter which affected the ratio and velocity of phase transformation. By fitting the measured thermal expansion curve, the value of b for DP980 in this study can be judged as 0.035 and the final value of f was about 99.5%. Therefore, the retained austenite can be

Table 1 Temperature-dependent material properties of CuCr [35]

T [$^\circ\text{C}$]	λ	c	ρ	E	YS	α	ν	R
20	0.326	0.385	8.89	130	130	1.76E-05	0.3	2.2E-05
200	0.345	0.406	8.89	105	195	1.66E-05	0.3	3.8E-05
400	0.348	0.422	8.89	100	85	1.83E-05	0.3	4.9E-05
600	0.347	0.438	8.89	80	10	2.0E-05	0.3	6.5E-05
800	0.349	0.460	8.89	70	5	2.16E-05	0.3	8.2E-05

Table 2 Temperature-dependent material properties of DP980 [36]

T [$^\circ\text{C}$]	λ	c	ρ	E	ν	R
20	0.02596	0.4236	7.6	211.4	0.33	1.756E-04
200	0.02596	0.4236	7.6	202.1	0.33	–
400	0.02924	0.4964	7.6	184.2	0.33	–
600	0.03124	0.5884	7.6	159.0	0.33	–
1000	0.0314	0.83	7.6	106.9	0.33	1.169E-03

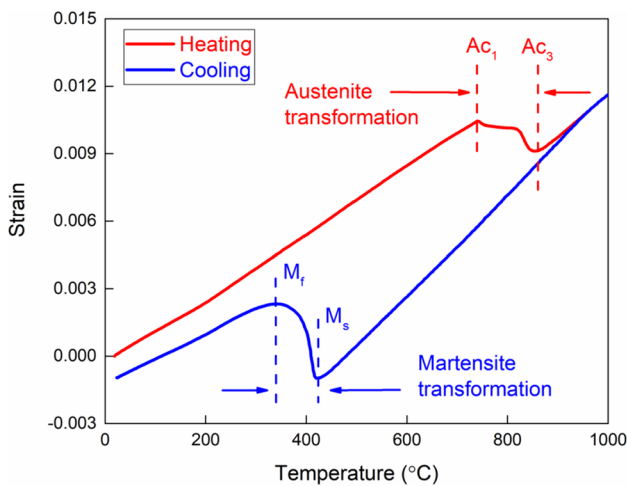


Fig. 7 Thermal expansion curve of DP980

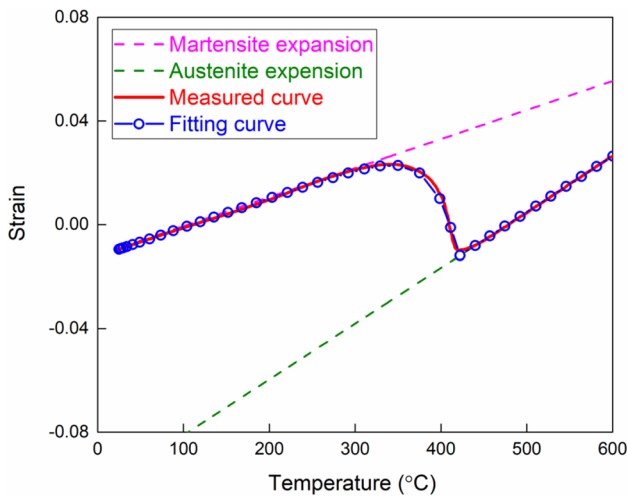
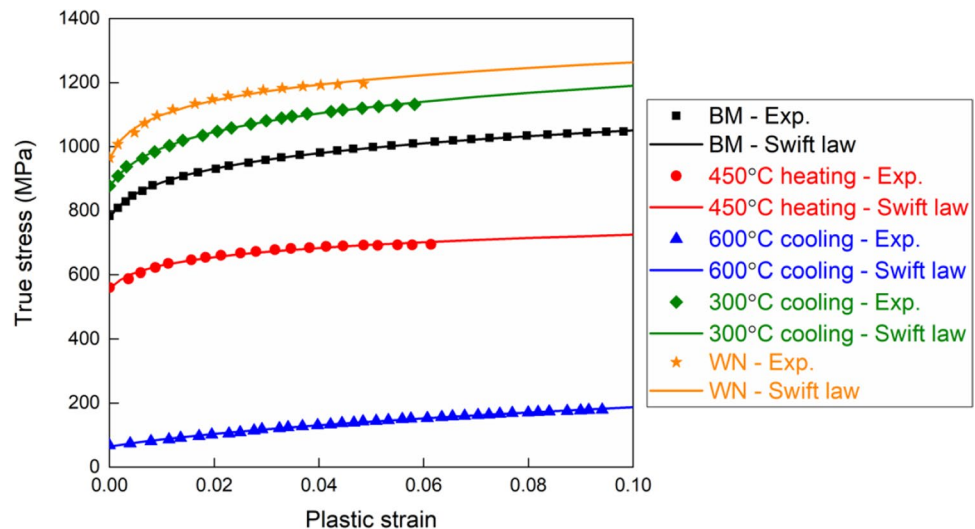


Fig. 8 Mathematical fitting result of the martensite transformation process

Fig. 9 Temperature-dependent true stress-plastic strain curve of DP980



ignored and the influence of transformation induced plastic (TRIP) was not taken into account in the present research. The fitting result is given in Fig. 8.

The true stress-effective plastic strain curves of DP980 at different temperatures are given in Fig. 9. The strain-hardening behaviors of different phases can be described and fitted via the Swift power law [34]:

$$\sigma = K(\epsilon_0 + \epsilon_p)^n \tag{15}$$

where σ was the flow stress, ϵ_p represented the effective plastic strain. K , ϵ_0 , and n expressed the strength coefficient, initial strain value, and strain-hardening exponent, respectively.

The yield strength and Swift law parameters of different phases are summarized in Table 3. The BM and WN are the abbreviation of base metal and welded nugget.

The yield strength of DP980 base metal was gauged as about 779MPa at room temperature. After heating and softening, the value decreased to about 557MPa at 450°C. When the metal cooled from 1000 to 600°C, the microstructure in DP980 was austenite, which had a much low yield strength (about 64MPa) and the strain-hardening tendency was also different with martensite. When the metal continued cooling to 20°C, the microstructure altered into as-welded martensite, which had a more coarse grain size and the yield strength increased to about 962MPa.

The temperature-dependent yield strength of different phases in DP980 was cited from reference [20] and calibrated by the measured results, as shown in Fig. 10. In the heating stage, the yield strength was varied along the initial martensite curve and transferred to the austenite curve between Ac1 and Ac3. In the cooling stage, the yield strength was changed along the austenite curve and altered to the as-welded martensite curve between Ms and Mf. The JWRIAN-Hybrid will judge the detailed phase according to transient temperature and then give relative properties

Table 3 The yield strength and Swift law parameters of different phases

Phases	Yield strength (MPa)	Swift law parameters		
		K (MPa)	ϵ_0	n
BM	779	1258	0.00238	0.079
450°C heating	557	843	0.00191	0.066
600°C cooling	64	516	0.01091	0.461
300°C cooling	875	1414	0.00293	0.086
WN	962	1461	0.00140	0.064

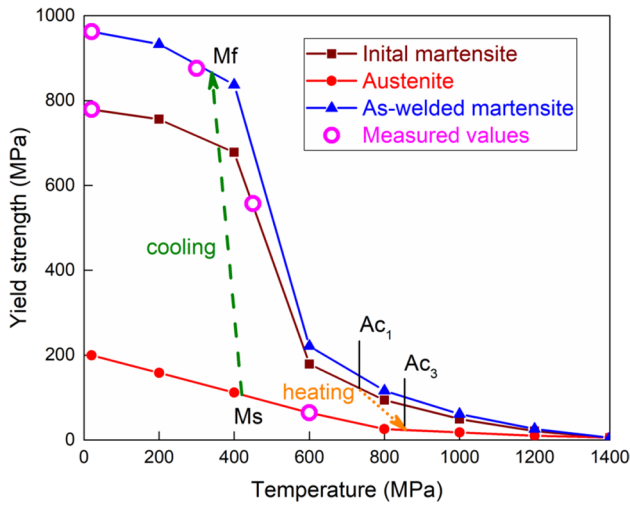


Fig. 10 Temperature-dependent yield strength of DP980 [20]

to the model. The true stress-plastic strain relationship of distinct phases in different temperatures was determined by the discrepancy of yield strength with measured one. It should be mentioned that the yield strength of mixed phase was calculated according to the following equation:

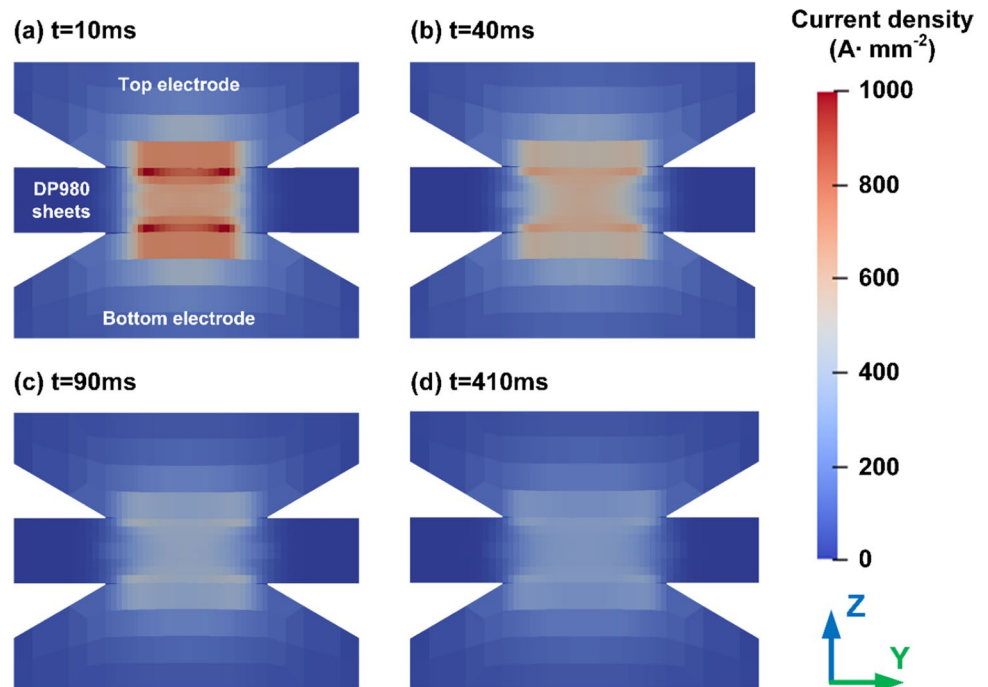
$$\sigma_{\alpha}^Y = f_m(T, T_p) \cdot \sigma_I^Y + [1 - g(T_p)] \cdot \sigma_W^Y + [1 - f_m(T, T_p)] \cdot \sigma_Y^Y \quad (16)$$

where σ_{α}^Y was the yield strength of mixed phase; σ_I^Y , σ_W^Y , and σ_Y^Y represented the yield strength of initial martensite, as-welded martensite, and austenite, respectively. $f_m(T, T_p)$ was a no-linear function to calculate the martensite fraction based on the transient temperature T and peak temperature T_p . $g(T_p)$ was a piecewise function related to Ac_1 and Ac_3 .

4.2 Results of electrical and thermal analysis

The predicted current density distribution is shown in Fig. 11. The transient situation at the start of first current pulse is depicted in Fig. 11a. There were significant current concentrations at the edge of contact zone between electrodes and steel sheets. The contact region between two welded sheets was relatively larger thereby the current density was smaller on the steel/steel interface. During the first pulse, the metal was heated and softened rapidly. The contact condition was improved with the contact region expanding. Therefore, the current density distribution on

Fig. 11 Predicted current density distribution



the electrode/sheet interface was more uniform at the end of first current pulse, as depicted in Fig. 11b.

The second current was employed to support the growth of welding nugget so the welding current was lower. In Fig. 11c, d, the current density presented a low magnitude and the contact conditions in three interfaces were almost same at the end of the entire heating process.

The temperature field during the whole welding process is given in Fig. 12. At the start of heating, Joule heat was generated on the interfaces between electrodes and sheets due to large contact electrical resistance, as depicted in Fig. 12a. During the first current pulse, the welding nugget appeared and grew up. In Fig. 12d, the short cooling stage between two current pulses led to the shrinkage of temperature field. The maximum temperature in welded zone was lower than the melting temperature of DP980 (about 1450°C), which demonstrated that the molten zone disappeared temporarily. During the second current pulse, only the dimension of welding nugget increased but its overall shape was not changed clearly since the contact condition was better and more stable, as shown in Fig. 12e. In Fig. 12f, the molten zone reached its largest size at the end of heating and then cooled to room temperature after welding. During the double-pulse RSW process, the welding nugget disappeared and reappeared for the short interval between two pulses. Only the molten zone of the second current pulse can cool to room temperature rapidly. Therefore, the peak temperature distribution of the second current pulse described the final profile of welding nugget. The variation of welding nugget size during heating process is given in Fig. 13.

In the present research, molten zone morphology on cross-section of welded joint was employed to verify the prediction of temperature field, as shown in Fig. 14. One can find the welding nugget clearly via the coarse columnar crystals which grew perpendicular to the boundary. And the HAZ was located on the outside of welding nugget. Compared with the macroprofile of cross-section on welded joints, the predicted temperature field can present similar contours for both welding nugget and HAZ, which

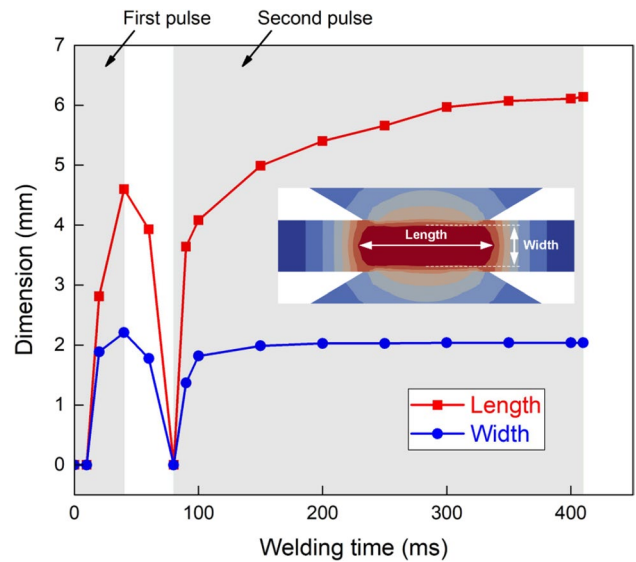


Fig. 13 The variation of welding nugget size

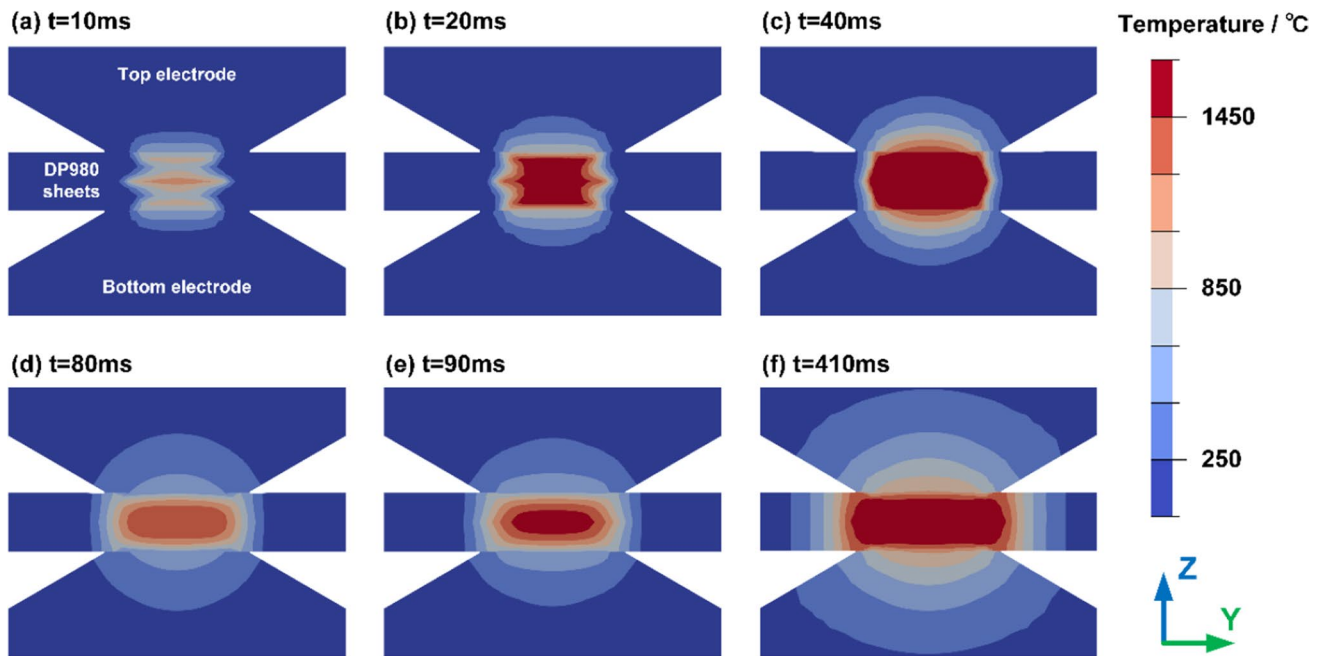


Fig. 12 Predicted temperature field and its change in the entire welding process

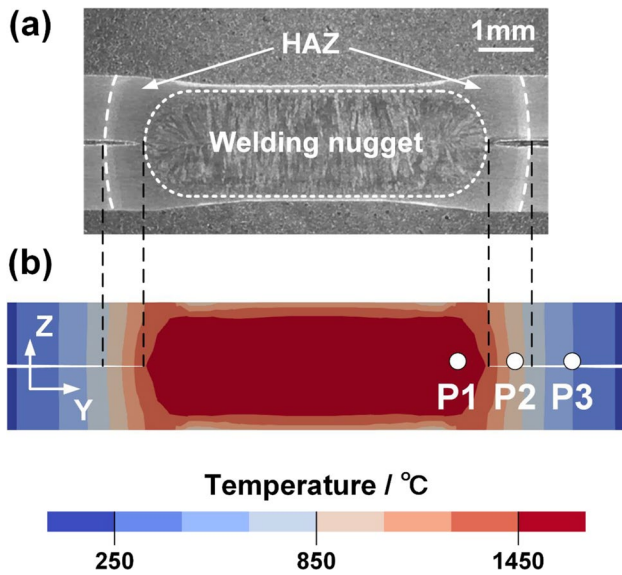


Fig. 14 Comparison of the molten zone morphology with the predicted temperature field

demonstrated that the in-house FE code JWRIAN-RSW can analyze the electrical-thermal process of RSW accurately.

The thermal cycles of three positions marked in Fig. 14b are summarized in Fig. 15a. The P1 was located at the edge of welding nugget, whose peak temperature was higher than the melting temperature of steel. Since P1 was close to the center zone, its thermal cycle was significantly affected by the short cooling between two current pulses, which was reflected as the apparent temperature drop in heating stage. The local microstructure was coarse martensite, as shown in Fig. 15b. The peak temperature of P2 in HAZ was higher than A_{c3} but much lower than 1450°C . Therefore, the metal in P2 was not melted while the SSPT appeared here. Such a thermal history can lead to the variation of microstructure. One can also find the martensite in Fig. 15c. For P3, which was located in the base metal, its thermal cycle was not high enough to trigger the phase transformation. The microstructure was maintained in the original condition in this region, which included martensite and ferrite, as presented in Fig. 15d.

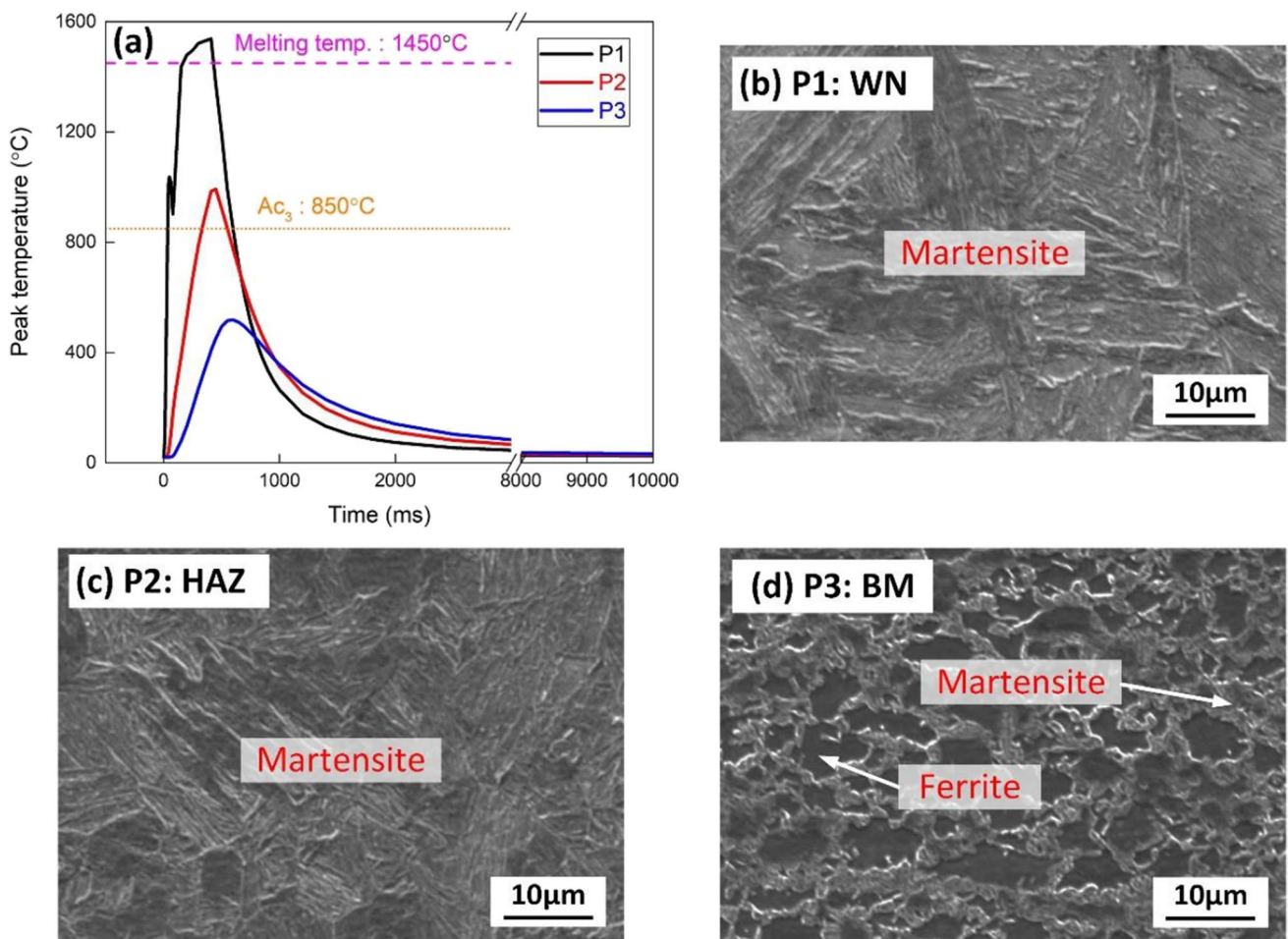


Fig. 15 a Predicted thermal cycle and microstructure on b welding nugget, c HAZ, and d BM

4.3 Results of mechanical analysis

The mechanical analysis was performed subsequently with considering the metallurgical behaviors of DP980 to predict the welding residual stress. The present research pays more attention to the X-stress (hoop stress) in the RSWed joints, whose entire evolution is depicted in Fig. 16.

The initial stress in DP980 sheets was almost zero; hence, it was ignored in the numerical modeling. At the start of welding, the electrode pressure and thermal expansion of metal led to compressive stress in the welding nugget, as shown in Fig. 16b. Meanwhile, the contact condition was poor between metal sheets. The large Joule heat generation introduced high temperature here; thereby, the softened metal presented a low-stress value at the center of nugget. In the continuous heating process, as depicted in Fig. 16c, d, the dimension of molten zone increased and the local stress was almost zero. At the outside of molten zone, the heated metal generated compressive stress and small tensile stress can be observed further away due to the stress balance.

In the cooling stage, the temperature was decreased and austenite would transfer into martensite accompanied with the volume change and yield strength variation. In Fig. 16e, the apparent compressive stress appeared on the surface of welding nugget previously, which indicated the martensite transformation occurred here since the connection with electrode led to rapid cooling. Although the martensite transformation can introduce volume expansion and contribute

to compressive stress, it would stop at a relatively high temperature (about 340°C). During the continuous cooling, the shrinkage of martensite still caused significant tensile stress in welding nugget and HAZ, as illustrated in Fig. 16f, g. Due to work hardening, the maximum tensile stress can reach about 1050MPa. After springback, the constraint and pressure of electrodes were removed. A part of elastic strain was released; therefore, the sizeable tensile stress in welding nugget became lower. The final value on surface was about 300MPa. Due to the global stress equilibrium, the compressive stress of about –120MPa can be obtained at the edge of sheets. Besides, the notches outside the edge of lapped sheets represented the indentation of electrodes, which was induced by the metal softening and electrode pressure.

The evolution of Y-stress, which is equivalent to the radial stress, is depicted in Fig. 17. Generally, the Y-stress presented a similar evolution to the X-stress. There was always compressive stress outside the molten zone. The low tensile stress was generated in welding nugget and HAZ after martensite transformation, which grew up to its peak value during the continuous cooling and then decreased significantly after springback. However, the distribution of Y-stress was complicated in the cross-section since the global stress equilibrium was more complex. Finally, there was low tensile stress about 240MPa at the center of surface.

Figure 18 presents the comparison of predicted and measured residual stress distribution on the surface of RSWed joint. Obviously, the springback process must be considered

Fig. 16 The X-stress evolution on the cross-section of welded joint

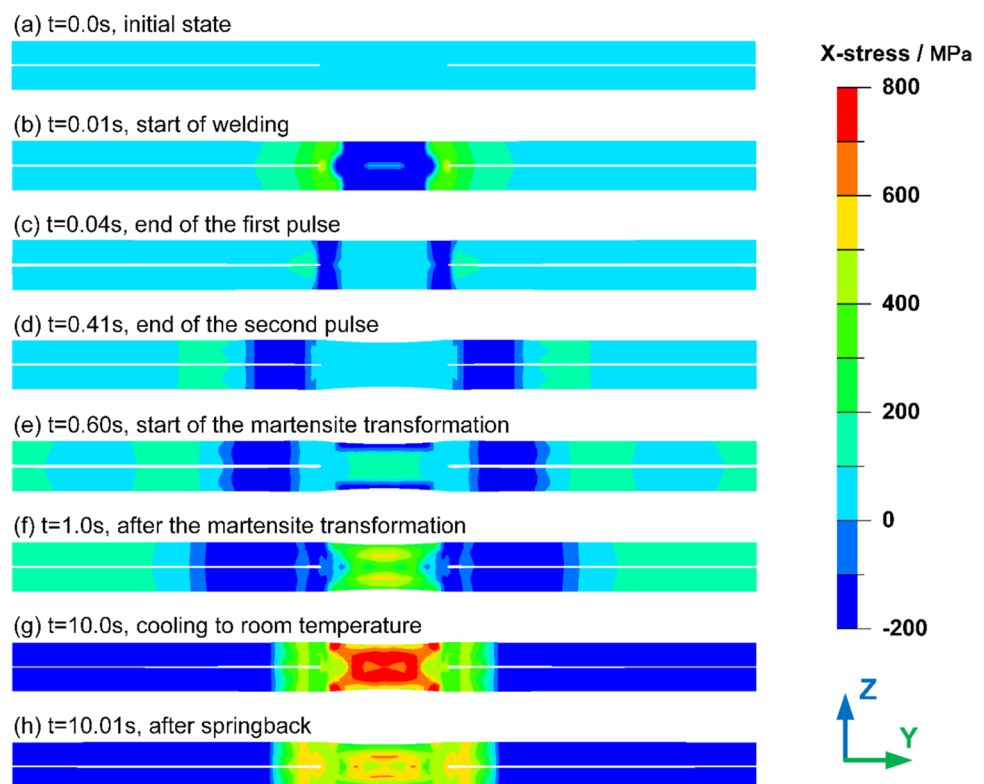
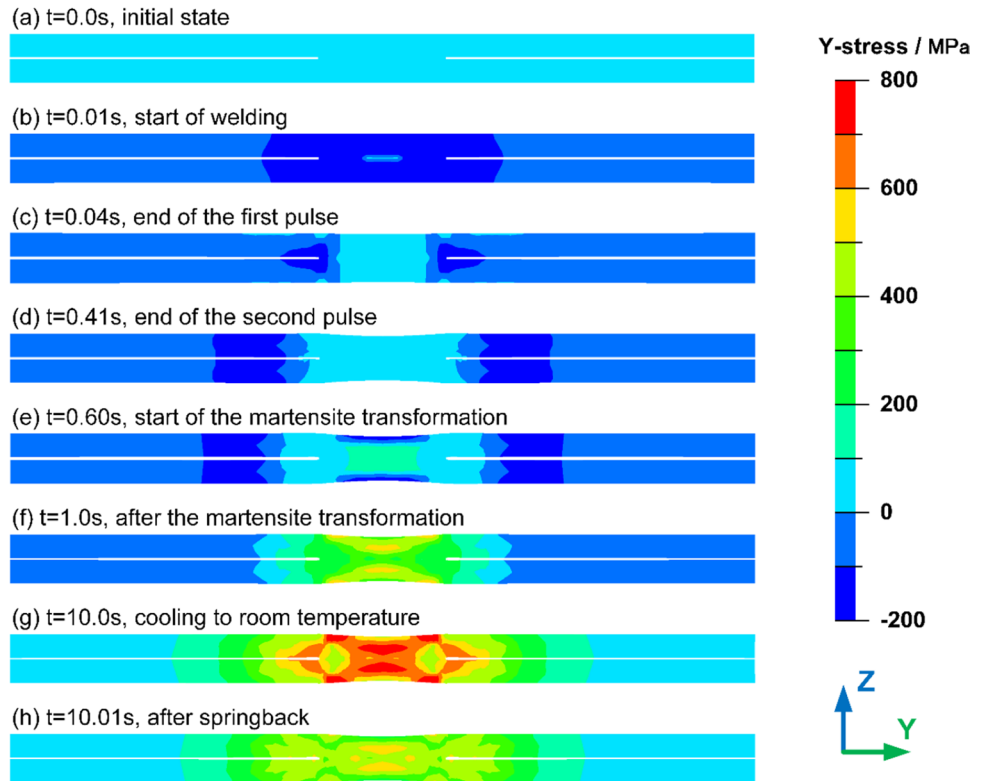


Fig. 17 The Y-stress evolution on the cross-section of welded joint



in the numerical analysis of welding residual stress in order to ensure accuracy. One can find significant peaks at the edge of electrode indentation, which indicated the effect of stress concentration and constraints. Generally, the predicted residual stress tendency showed good agreement with the XRD measurements. It demonstrated that the developed numerical model was effective in predicting the welding residual stress in DP980 with considering SSPT and springback.

5 Conclusions

In the present research, the DP980 sheets were joined via resistance spot welding. The electrical-thermal-metallurgical-mechanical coupled process of RSW was modeled numerically by the in-house FE code JWRIAN-RSW and JWRIAN-Hybrid. High-temperature material properties of DP980 were clarified by experiments to improve the

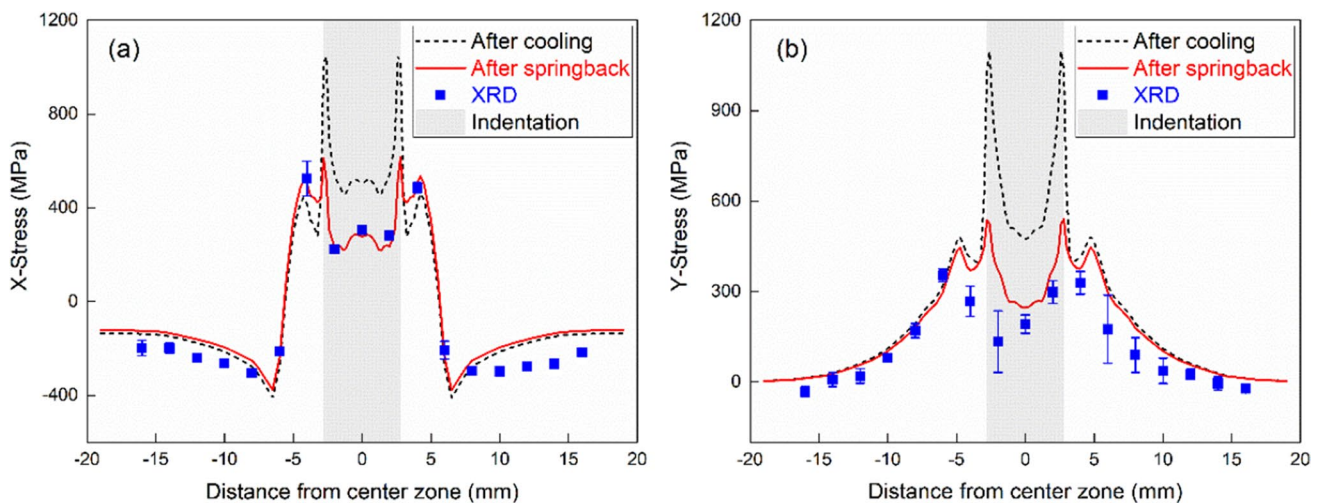


Fig. 18 Comparison of the prediction and measurement of residual stress distribution

simulation accuracy. The effects of both solid-state phase transformation and springback process were taken into account. The predicted temperature field and residual stress distribution were verified by the molten zone morphology and XRD measurement, respectively. The following conclusions can be drawn:

- 1) The integrated FEM model of JWRIAN-RSW and JWRIAN-Hybrid was effective in reproducing the multi-physics coupled process of resistance spot welding. The predicted molten zone and residual stress distribution showed good agreement with the experimental measurements.
- 2) The law parameter b in K-M equation for the martensite transformation was identified to be 0.035 for DP980.
- 3) The molten zone disappeared during the short cooling between two current pluses and reappeared in the continuous heating, whose final dimension was determined by the second current pulse majorly.
- 4) There was a significant stress drop on the center of welding nugget surface, which represented the contribution of volume expansion during martensite transformation. The final X-stress (hoop stress) and Y-stress (radial stress) were about 300MPa and 240MPa, respectively.
- 5) The tensile stress in welding nugget was decreased clearly since a part of elastic strain was released after unloading the pressure and constraints of electrodes. It was critical to consider the springback process in the numerical model of RSW to predict residual stress accurately.

Code availability Not applicable

Author contribution Sendong Ren: conceptualization, software, writing original draft; Wenjia Huang: investigation; Ninshu Ma: conceptualization, software, supervision; Goro Watanabe: project administration, validation; Zhengguang Zhang: data curation; Wenze Deng: resources.

Funding This research was financially supported by joint research project between Geely Automobile Research Institute (Ningbo) Co., Ltd. and Osaka University.

Data availability The datasets used or analyzed during the current study are available within the article.

Declarations

Ethics approval Not applicable.

Consent to participate Not applicable.

Consent for publication All the authors agreed to publish this paper.

Conflict of interest The authors declare no competing interests.

References

1. Mohamad Junaida LH, Sakundarini N (2021) Material selection for lightweight design of vehicle component. Springer Singapore, Singapore, pp 1001–1015
2. Kuziak R, Kawalla R, Waengler S (2008) Advanced high strength steels for automotive industry. Archives of Civil and Mechanical Engineering 8(2):103–117
3. Aslanlar S (2006) The effect of nucleus size on mechanical properties in electrical resistance spot welding of sheets used in automotive industry. Mater Des 27(2):125–131
4. Pouranvari M, Marashi S (2013) Critical review of automotive steels spot welding: process, structure and properties. Sci Technol Weld Join 18(5):361–403
5. Vijayan V, Murugan SP, Ji C, Son S-G, Park Y-D (2021) Factors affecting shrinkage voids in advanced high strength steel (AHSS) resistance spot welds. J Mech Sci Technol 35(11):5137–5142
6. Ashiri R, Shamanian M, Salimijazi HR, Haque MA, Bae J-H, Ji C-W, Chin K-G, Park Y-D (2016) Liquid metal embrittlement-free welds of Zn-coated twinning induced plasticity steels. Scr Mater 114:41–47
7. Qi L, Li F, Chen R, Zhang Q, Li Y (2020) Improve resistance spot weld quality of advanced high strength steels using bilateral external magnetic field. J Manuf Process 52:270–280
8. Ren D, Zhao D, Zhao K, Liu L, He Z (2019) Resistance ceramic-filled annular welding of DP980 high-strength steel. Mater Des 183:108118
9. Yang Y-S, Son K-J, Cho S-K, Hong S-G, Kim S-K, Mo K-H (2001) Effect of residual stress on fatigue strength of resistance spot weldment. Sci Technol Weld Join 6(6):397–401
10. Sato A, Hashimoto T, Nishikawa I, Iyota M (2019) A study on X-ray residual stress measurement to surface of resistance spot welds. Transactions of Society of Automotive Engineers of Japan 50(2)
11. Chabok A, van der Aa E, Basu I, De Hosson J, Pei Y (2018) Effect of pulse scheme on the microstructural evolution, residual stress state and mechanical performance of resistance spot welded DP1000-GI steel. Sci Technol Weld Join 23(8):649–658
12. Moshayedi H, Sattari-Far I (2012) Numerical and experimental study of nugget size growth in resistance spot welding of austenitic stainless steels. J Mater Process Technol 212(2):347–354
13. Wan H, Wang M, Wang BE, Carlson DRS (2016) Numerical simulation of resistance spot welding of Al to zinc-coated steel with improved representation of contact interactions. Int J Heat Mass Transf 101:749–763
14. Ma N, Murakawa H (2010) Numerical and experimental study on nugget formation in resistance spot welding for three pieces of high strength steel sheets. J Mater Process Technol 210(14):2045–2052
15. Lee Y, Jeong H, Park K, Kim Y, Cho J (2017) Development of numerical analysis model for resistance spot welding of automotive steel. J Mech Sci Technol 31(7):3455–3464
16. Wang B, Hua L, Wang X, Song Y, Liu Y (2016) Effects of electrode tip morphology on resistance spot welding quality of DP590 dual-phase steel. Int J Adv Manuf Technol 83(9-12):1917–1926
17. Zhao D, Wang Y, Zhang P, Liang D (2019) Modeling and experimental research on resistance spot welded joints for dual-phase steel. Materials 12(7):1108
18. Feujofack Kemda B, Barka N, Jahazi M, Osmani D (2021) Modeling of phase transformation kinetics in resistance spot welding and investigation of effect of post weld heat treatment on weld microstructure. Met Mater Int 27(5):1205–1223
19. Iyota M, Mikami Y, Hashimoto T, Taniguchi K, Ikeda R, Mochizuki M (2013) The effect of martensitic transformation on residual stress in resistance spot welded high-strength steel sheets. J Alloys Compd 577:S684–S689
20. Pakkanen J, Vallant R, Kičičin M (2016) Experimental investigation and numerical simulation of resistance spot welding for

- residual stress evaluation of DP1000 steel. *Welding in the World* 60(3):393–402
21. Li S, Ren S, Zhang Y, Deng D, Murakawa H (2017) Numerical investigation of formation mechanism of welding residual stress in P92 steel multi-pass joints. *J Mater Process Technol* 244:240–252
 22. Appuhamy J, Ohga M, Kaita T, Fujii K, Dissanayake P (2011) Development of analytical method for predicting residual mechanical properties of corroded steel plates. *International Journal of Corrosion* 2011
 23. Ueda Y, Murakawa H, Ma N (2012) *Welding deformation and residual stress prevention*. Elsevier
 24. Ren S, Ma Y, Ma N, Saeki S, Iwamoto Y (2021) 3-D modelling of the coaxial one-side resistance spot welding of AL5052/CFRP dissimilar material. *J Manuf Process* 68:940–950
 25. Ren S, Ma Y, Saeki S, Iwamoto Y, Ma N (2020) Numerical analysis on coaxial one-side resistance spot welding of Al5052 and CFRP dissimilar materials. *Mater Des* 188:108442
 26. Li Y, Lin Z, Shen Q, Lai X (2011) Numerical analysis of transport phenomena in resistance spot welding process. *J Manuf Sci Eng* 133(3)
 27. Li Y, Wei Z, Li Y, Shen Q, Lin Z (2013) Effects of cone angle of truncated electrode on heat and mass transfer in resistance spot welding. *Int J Heat Mass Transf* 65:400–408
 28. Nishimura R, Ma N, Liu Y, Li W, Yasuki T (2021) Measurement and analysis of welding deformation and residual stress in CMT welded lap joints of 1180 MPa steel sheets. *J Manuf Process* 72:515–528
 29. Ma N (2016) An accelerated explicit method with GPU parallel computing for thermal stress and welding deformation of large structure models. *Int J Adv Manuf Technol* 87(5):2195–2211
 30. Deng D, Murakawa H (2006) Prediction of welding residual stress in multi-pass butt-welded modified 9Cr–1Mo steel pipe considering phase transformation effects. *Comput Mater Sci* 37(3):209–219
 31. Zhang F, Ruimi A, Wo PC, Field DP (2016) Morphology and distribution of martensite in dual phase (DP980) steel and its relation to the multiscale mechanical behavior. *Mater Sci Eng A* 659:93–103
 32. Ren S, Li S, Wang Y, Deng D, Ma N (2019) Predicting welding residual stress of a multi-pass P92 steel butt-welded joint with consideration of phase transformation and tempering effect. *J Mater Eng Perform* 28(12):7452–7463
 33. Krauss G, Krauss G (1989) *Steels: heat treatment and processing principles*. ASM international Materials Park, OH
 34. Swift HW (1952) Plastic instability under plane stress. *Journal of the Mechanics and Physics of Solids* 1(1):1–18
 35. Matula RA (1979) Electrical-resistivity of copper, gold, palladium, and silver. *J Phys Chem Ref Data* 8(4):1147–1298
 36. Lee E-H, Yang D-Y, Yoon JW, Yang W-H (2015) Numerical modeling and analysis for forming process of dual-phase 980 steel exposed to infrared local heating. *Int J Solids Struct* 75-76:211–224

Publisher's note Springer Nature remains neutral with regard to jurisdictional claims in published maps and institutional affiliations.

Springer Nature or its licensor (e.g. a society or other partner) holds exclusive rights to this article under a publishing agreement with the author(s) or other rightsholder(s); author self-archiving of the accepted manuscript version of this article is solely governed by the terms of such publishing agreement and applicable law.